

Modeling line profile variations of σ Ori E and θ^1 Ori C

A. Reiners¹, O. Stahl¹, B. Wolf¹, A. Kaufer², and T. Rivinius^{2*}

¹ Landessternwarte Heidelberg, Königstuhl, 69117 Heidelberg, Germany (A.Reiners@lsw.uni-heidelberg.de)

² European Southern Observatory, Karl-Schwarzschild-Strasse 2, 85748 Garching bei München, Germany

Received 20 March 2000 / Accepted 8 September 2000

Abstract. We analyse phase-dependent variations of the photospheric lines of the magnetic B star σ Ori E and the suspected magnetic O star θ^1 Ori C. In the framework of the oblique magnetic rotator model, the observations are interpreted as the result of inhomogeneous chemical abundances – spots – at the stellar surface. This model can at least qualitatively explain the line profile variations with two spots at the magnetic poles of both stars. In the case of σ Ori E, we find the spots to be overabundant in He and depleted in metals. For θ^1 Ori C the presumed spots would be depleted both in He and in metals. For θ^1 Ori C we also discuss an alternative model with spots of enhanced abundances at the magnetic equator. This model better fits the observations. Chemical fractionation is not expected for θ^1 Ori C and the absorption lines show indications of circumstellar absorption. Therefore, the most likely interpretation of the variations observed in the absorption lines of this star is the presence of excess absorption in a circumstellar cloud and not that of a difference in chemical abundance.

Key words: stars: chemically peculiar – stars: early-type – stars: individual: σ Ori E – stars: individual: θ^1 Ori C – stars: magnetic fields – stars: statistics

1. Introduction

Periodic line profile variability is a common feature in magnetic early-type stars. In most of these objects, the generally accepted interpretation of these variations is rotational modulation caused by inhomogeneities in the element abundances at the surface. The abundance patterns usually follow magnetic surface structures, e.g. the magnetic poles, which then gives rise to rotational modulation, if the magnetic and the rotational axis are inclined. This is the oblique magnetic rotator model. One of the hottest of the established magnetic stars is σ Ori E (=HD 37479, HR 1932, spectral type B2Vp), a He-variable star. σ Ori E is also one of the best-studied of the variable chemically peculiar B stars (see e.g. Groote & Hunger 1997).

Send offprint requests to: A. Reiners

* Based on observations collected at the European Southern Observatory, La Silla, Chile

Periodic spectral variations in some emission lines in the well-known young O star θ^1 Ori C (=HD 37022, HR 1895, spectral type O6pe) were first detected by Stahl et al. (1993). Later Stahl et al. (1996) found that the photospheric absorption lines are also variable, with the same period of about 15 days. The stellar wind lines in the UV (Walborn & Nichols 1994) and the X ray emission (Gagné et al. 1997) are also variable with the same period.

Although θ^1 Ori C is much hotter than any of the classical magnetic A and B stars, the observed variations are reminiscent of these stars. Attempts to measure a magnetic field in θ^1 Ori C were unsuccessful (Donati & Wade 1999). The derived upper limits are so high, however, that this does not exclude a magnetic origin of the variations. Babel & Montmerle (1997) could quantitatively explain the X-ray flux and variability with a model of a magnetically confined wind shock. This gives strong support to a magnetic origin for the variability of θ^1 Ori C. This star is of particular interest, since it is by far the hottest object known which shows such strictly periodic variations. It could represent an extension of magnetic stars to the O star range.

In this paper we model the variations of the photospheric lines of θ^1 Ori C with surface spots of different element abundances. As a comparison object we also model the magnetic star σ Ori E. In this star, a magnetic origin of the variations is undisputed. The aim of the present paper is to investigate whether the variations observed for θ^1 Ori C can be explained, in analogy to σ Ori E, by chemical abundance variations at the surface or whether an other mechanism is needed.

2. Observations and data reduction

The observations were carried out with FEROS at the ESO 1.52-m telescope in La Silla. FEROS (Fiber-fed Extended Range Optical Spectrograph) is a bench-mounted fiber-linked echelle spectrograph located in the former Coudé room of the 1.52-m telescope. FEROS has no moving parts and is located in a temperature and humidity-controlled room, which allows for very stable operation.

The instrument is designed for high-dispersion spectroscopy with a resolution of $\lambda/\Delta\lambda = 48\,000$, covering the spectral range from 3700–9200 Å in one exposure. FEROS is equipped with a $2k \times 4k$ $15\mu\text{m}$ pixel CCD. The high resolution is achieved

Table 1. FEROS-spectra of σ Ori E. The phases were calculated with the period of $P = 1.19084$ days and the epoch $MJD = JD - 2,400,000.5 = 42\,778.319$

Sp. No.	Phase	Date	MJD
0935	0.749	11/16/1998	51134.145
0949	0.817	11/16/1998	51134.227
0955	0.940	11/16/1998	51134.371
1006	0.721	11/17/1998	51135.301
1013	0.771	11/17/1998	51135.359
1148	0.359	11/19/1998	51137.254
1209	0.294	11/20/1998	51138.367
1246	0.071	11/21/1998	51139.293
1295	0.937	11/22/1998	51140.320
1336	0.804	11/23/1998	51141.355
1370	0.579	11/24/1998	51142.277
1421	0.401	11/25/1998	51143.258
1465	0.225	11/26/1998	51144.238
1513	0.078	11/27/1998	51145.254
1600	0.757	11/29/1998	51147.254
1636	0.550	11/30/1998	51148.195
1676	0.414	12/01/1998	51149.227
1716	0.213	12/02/1998	51150.176
1763	0.102	12/03/1998	51151.234
1770	0.163	12/03/1998	51151.309
1773	0.198	12/03/1998	51151.352
1791	0.843	12/04/1998	51152.117
1801	0.903	12/04/1998	51152.191
1840	0.614	12/05/1998	51153.039
1909	0.503	12/06/1998	51154.097
1985	0.223	12/08/1998	51156.145
2414	0.181	12/27/1998	51175.148

by an image slicer (Kaufer 1998) which increases the spectral resolution by a factor of two.

FEROS uses two fibers simultaneously. One fiber contains the object spectrum. The second fiber can contain either the sky spectrum or the simultaneously exposed spectrum of a ThArNe-calibration lamp. The latter mode is intended for highest accuracy in radial velocity measurements and was not used in our observations. A more detailed description is given by Kaufer et al. (1997) and Kaufer and Pasquini (1998).

For a complete and fully automatic reduction of the data a special data reduction software was developed. It is implemented as a context in ESO-MIDAS. Fully automatic reduction for preview data is done on-line at the telescope. The reduction can include optimum extraction, following the method of Mukai (1990). Maximum signal-to-noise ratio (S/N) is achieved by choosing optimum weights for the summation of the pixel values. This procedure also allows removal of cosmic ray hits. The wavelength calibration is done by a global fit formula, which calibrates all echelle orders simultaneously. For details of the reduction procedure see Stahl et al. (1999).

The data of σ Ori E were taken during November and December 1998, partly during the commissioning phase of FEROS. Note that the data from the commissioning phase are public and can be obtained from:

<http://www.lsw.uni-heidelberg.de/~akauffer/Feros/>

Table 2. FEROS-spectra of θ^1 Ori C. The phases were calculated with the period of $P = 15.422$ days and the epoch $MJD = JD - 2,400,000.5 = 48\,832.5$

Sp. No.	Phase	Date	MJD
7823	0.760	07/14/1999	51373.431
8146	0.214	07/21/1999	51380.436
8213	0.279	07/22/1999	51381.437
8320	0.344	07/23/1999	51382.439
8384	0.409	07/24/1999	51383.432
8455	0.473	07/25/1999	51384.428
8522	0.539	07/26/1999	51385.435
8580	0.604	07/27/1999	51386.446
8671	0.798	07/30/1999	51389.433
8726	0.864	07/31/1999	51390.454
8780	0.928	08/01/1999	51391.447
8897	0.990	08/02/1999	51392.400
8954	0.058	08/03/1999	51393.450
9015	0.122	08/04/1999	51394.435

θ^1 Ori C was observed in July and August of 1999. For σ Ori E and θ^1 Ori C, exposure times of 15 min and of 6 min, respectively, were typically used. The S/N of the extracted spectra depends on the wavelength and peaks at about 4500-5000 Å. In good conditions the typical peak S/N ratio is 250 and 300 for σ Ori E and θ^1 Ori C, respectively.

Many of the observations of σ Ori E have been done during the commissioning phase of FEROS, and part of the spectra are of poor quality. The two worst spectra were omitted for this work. In total, 27 spectra of σ Ori E were used; they are listed in Table 1.

14 spectra of θ^1 Ori C were obtained in 1999 and are listed in Table 2.

3. Synthetic spectra and line profile variations

We modeled the stellar surface with a modified version of the program developed and described by Townsend (1997a, 1997b). This package was originally developed for modeling rapidly rotating non-radially pulsating stars. For our purpose, we switched off the non-radial pulsations and modified the program to handle spots on the star instead. The modifications allow for local differences of element abundances.

The stellar surface is divided into a grid consisting of about 51 000 points. For each point, a local line profile has to be specified. We derived these line profiles by interpolating in a grid of line profiles derived in the following way: The model atmosphere structures were computed with ATLAS9 (Kurucz 1979, 1993). Line profiles were calculated with these model atmospheres using the BHT code (Baschek et al. 1966). With this code it is possible to modify the abundances of He and metals. For the He I lines the broadening theories of Griem et al. (1966) (He I $\lambda 4713$) and Barnard et al. (1974) (He I $\lambda 4471$, 4921) were used. Our grid of profiles covers the whole range of T_{eff} , $\log g$ and ϵ_{Ion} which occur at the stellar surface.

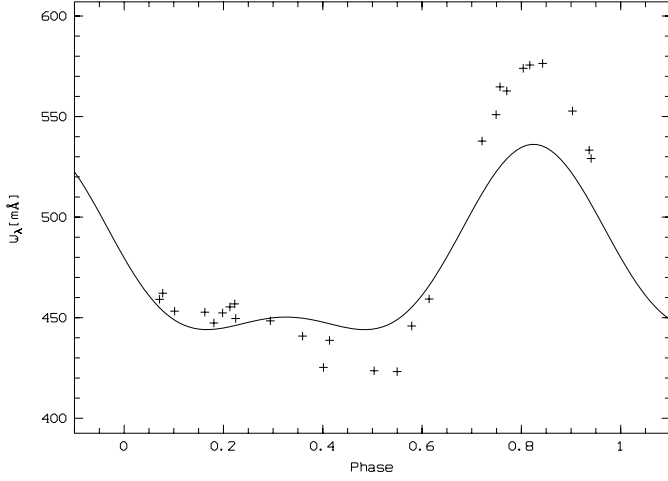


Fig. 1. Equivalent width of the He I $\lambda 4713$ line of σ Ori E versus phase (for a period of 1.19084 d and an epoch of $MJD = 42778.319$). The curve shows the equivalent width computed from the model.

Input parameters for the modeling of the complete surface are the polar radius R_{pol} , the polar effective temperature T_{eff} , the stellar mass M , the equatorial rotational velocity v_{rot} and the inclination of the rotation axis i . For each surface point T_{eff} , $\log g$, v_{proj} (the rotational velocity projected towards the observer) and μ (the angle under which the surface element is seen) are calculated. Rotational flattening and the dependence of temperature and gravity on stellar latitude (von Zeipel 1924) are taken into account. The element abundance ϵ_{Ion} is specified for each surface element. In this way, abundance spots at the surface are modeled.

The effect of rotation is simulated by modeling 20 snapshots of the star during one rotational cycle. The visible points of the stellar surface and their contribution to the flux are determined and integrated for each frame using the line profiles interpolated from the grid of line profiles computed with BHT.

In contrast to the analysis applied by Groote & Hunger (1997) – where the equivalent widths were calculated directly – we first synthesized the spectra and afterwards measured their equivalent widths. This procedure allows us to investigate variations in the line profiles as well as to compare the integrated equivalent widths.

4. σ Ori E

A crucial parameter needed to model the line profile variations is the rotational velocity. For determination of $v \sin i$, the line C II $\lambda 4267$ was used. This line is a close blend, but this does not affect the determination of $v \sin i$. To take care of the intrinsic variations in the line profile, the maximum flux spectrum of the series was used instead of an individual spectrum. A rotational profile was fitted to the spectrum. We derive $v \sin i = (140 \pm 10) \text{ km s}^{-1}$, which is in good agreement with previous works.

With the period of $P = 1.19$ d and a stellar radius of $R = 5.3 R_{\odot}$ (Groote & Hunger 1982) this leads to $v_{\text{rot}} = (225 \pm 50) \text{ km s}^{-1}$ and $i = (39 \pm 10)^{\circ}$.

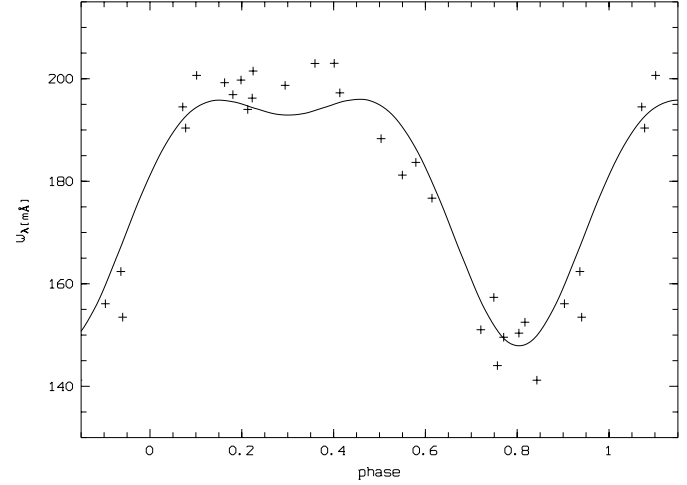


Fig. 2. Same as Fig. 1 but for the C II $\lambda 4267$ line.

In order to extract the equivalent width of the lines we fitted a Lorentzian profile of the shape

$$f(\lambda) = 1 - a \left[1 + \left(\frac{2(\lambda - b)}{c} \right)^2 \right]^{-1} \quad (1)$$

to the data. The local continuum is fitted with a straight line. The equivalent width then is derived from an integration of the fitted profile. In this way, the scatter in the equivalent width measurements is smaller than by direct integration. In Figs. 1 and 2 the equivalent widths of He I $\lambda 4713$ and C II $\lambda 4267$ are shown versus phase.

The long time basis of our equivalent width curves of He I $\lambda 4471$, combined with the data from other authors (Groote & Hunger 1997, 1977; Hunger et al. 1989), made it possible to improve the period of $P = (1.19081 \pm 0.00001) \text{ d}$ found by Hesser et al. (1977). We found the slightly different value of $P = (1.19084 \pm 0.00001) \text{ d}$.

If we assume that this period difference is due to a period change, we derive $\frac{\dot{P}}{P} = 2.7 \cdot 10^{-6} \text{ yr}^{-1}$ or $\tau = 2.3 \cdot 10^6 \text{ yr}$. (Note that the longer period is a mean over 22 years.) The rotational braking time due to angular-momentum loss in the wind can be estimated according to Brandt (1970, p.84). With a mass-loss rate of $\dot{M} \approx 10^{-10} M_{\odot} \text{ yr}^{-1}$ (Groote & Hunger 1997) a spin-down time of $\tau \approx 10^7 \text{ yr}$ is derived, using $I = kMR^2$ ($k \approx 0.09$, c.f. Mihalas & Conti 1980) and $r_0 = 30 R_{\star}$.

The results differ by one order of magnitude. Thus it seems indeed possible that the period difference might be due to spin-down. It should be noted, however, that the period given by Hesser et al. (1977) was derived from a time basis of 793 d only. Our period is based on data covering 22 yr. Both studies quote the same error for the period. We think that the error given by Hesser et al. (1977) is a bit optimistic and that the period difference might be an artefact.

In this paper we work with data covering only a span of 41 days and the influence on our work of such a small period-correction is negligible.

Table 3. Ion-abundances inside (ϵ_{spot}) and outside (ϵ_0) of the spots in our model. The parameters of obliquity, $\beta = 66^\circ$ (angle between the rotational and magnetic axes) and the sizes of the spots at the magnetic poles ($r_1 = 60^\circ$ and $r_2 = 60^\circ$) are the same for all elements. There is an offset of $\Delta\varphi = 25^\circ$ between them. In the spots, He is overabundant and the metals are depleted. The absolute abundances of the carbon line CII λ 4267 are known to be determined incorrectly by BHT (Kaufer et al. 1994). Their value is about 0.7 dex too low.

	HeI	CII	SiIII
ϵ_{spot}	12.0	7.0	7.2
ϵ_0	11.2	8.3	8.0

With the present set of parameters we have a complete stellar model of σ Ori E. For the Kurucz stellar atmospheres we adopted a polar temperature of $T = 22\,500$ K, $\log g = 3.95$ and $M = 8.9 M_\odot$. The only free parameter left is the abundance distribution of the elements.

The phase dependence of the equivalent widths shows two absorption maxima which are separated by approximately $\Delta\Phi \approx 0.5$. For simplicity we assumed a centered magnetic dipole with circular abundance spots at the poles. The spot sizes can be varied individually in the model. The poles are located at an angular distance β from the rotational poles. The element-abundances are assumed to be constant inside and outside the spots. It was not our aim to determine locations of abundance variations of orders of a few percent. The priority was to reproduce qualitatively the behaviour of the spectral lines versus phase. Therefore, we only varied the size and chemical abundance of the spots and the surrounding stellar surface, until a reasonable match in the observed and modeled time series was achieved.

We are mainly interested in the behaviour of He- and metal-lines. The lines HeI $\lambda\lambda$ 4471, 4713, 4921, CII λ 4267 and SiIII $\lambda\lambda$ 4552, 4567 were modeled. Four of them are shown in Figs. 3 and 4. The parameters used to model the profile variations are shown in Table 3. r_1 and r_2 are the radii of the two spots, ϵ_{spot} and ϵ_0 are the abundances inside and outside of the spots, respectively. The absolute abundances of the carbon line CII λ 4267 are known to be given incorrectly by BHT (Kaufer et al. 1994). Their value is about 0.7 dex too low.

Our model nicely reproduces the phase variations of the observed line profiles versus phase. The polar spots for all ions are of the same size on the stellar surface. In the caps, He is overabundant and the metals are depleted. There is an offset of $\Delta\Phi = 0.07$ between He- and metal-caps within error limits. This corresponds to a distance of the centres of the spots on the stellar surface of $\Delta\varphi = 25^\circ$. Also the different behaviour of the different HeI-lines is reproduced. The shape and velocity pattern of the modeled time-series spectra strongly depend on size and position of the spots. It is not very sensitive to the absolute abundance in the spots and in the vicinity.

After comparison of the time-series, the equivalent widths have been calculated as described above. The modeled equivalent widths variation of HeI λ 4713 and CII λ 4267 are shown as full drawn lines in Figs. 1 and 2. The model reproduces the

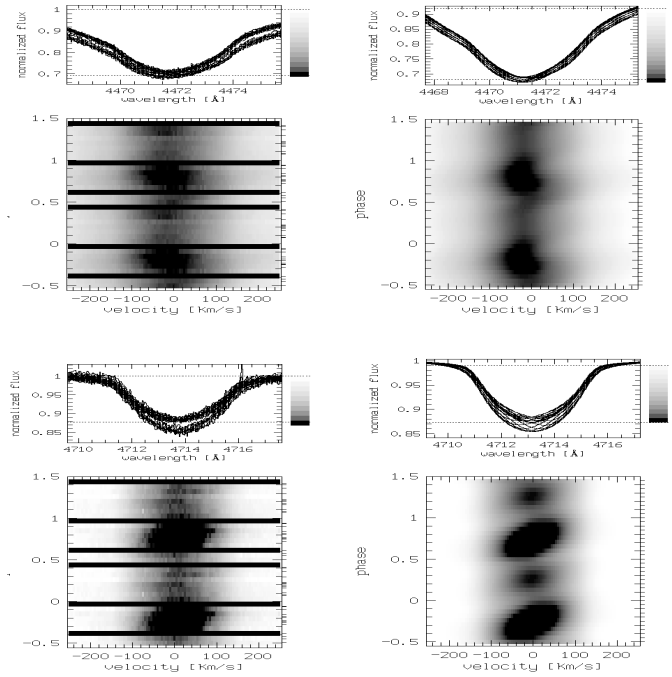


Fig. 3. Gray-scale representation of the profiles of HeI λ 4471 (top) and 4713 (bottom) of σ Ori E versus phase (left frames: observed data, right frames: model). Phases are from -0.5 to 1.5 with a bin size of 0.06 (data) and 0.05 (model), respectively. A velocity range of ± 250 km s $^{-1}$ around the rest wavelength is shown. Tick marks on the right border show phases where data have been taken.

tendency of the equivalent widths. For the carbon line it delivers an adequate fit to the data. HeI λ 4713 is not properly fitted. Fine-tuning has not been tried. Obviously, a slightly off-centered dipole could produce an even better fit. NLTE-effects may also play a role in the differences between model and data, especially for the HeI-lines but also for CII λ 4267.

Reproduction of the line-profiles means that the wings and core of the spectral lines at all phases are fitted correctly. The velocity distribution on the stellar surface at different times matches the model, i.e. no large scale motions other than rotation are present. Correspondence between the synthetic profile and the data is better than three percent of the continuum at all phases. No other simple model geometry was found to be able to reproduce the data equally well.

5. θ^1 Ori C

5.1. A polar spot model for θ^1 Ori C

θ^1 Ori C was first analysed in a similar way as σ Ori E. We determined the rotational velocity using the OIII λ 5592 line. With the high resolution of our data we are able to examine closely the line core, which is mostly unaffected by stellar wind effects. However, as can be seen in Fig. 5, the line profile shows significant deviations from a pure rotationally broadened photospheric profile. We find a value of (32 ± 5) km s $^{-1}$ for $v \sin i$ by fitting only the line core. This is much lower than earlier values derived

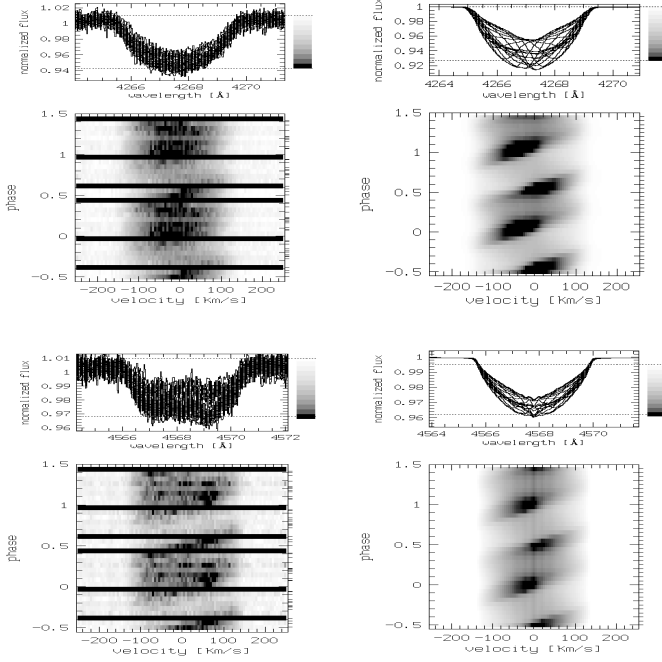


Fig. 4. Same as Fig. 3 but for CII λ 4267 (top) and SiIII λ 4567 (bottom).

using HeI and Balmer lines. Stahl et al. (1996) point out that this could be due to an unknown broadening mechanism in the HeI-lines. They found $v \sin i = 50 \text{ km s}^{-1}$ as an upper limit.

The stellar parameters of θ^1 Ori C are, except for the period, not well known. The period of $P = 15.422 \pm 0.002 \text{ d}$ found by Stahl et al. (1996) is confirmed by the new data. From $v \sin i = 32 \text{ km s}^{-1}$ and the period, we can determine the stellar radius, if the inclination of the rotation axis is known and the period is assumed to be due to rotation. Donati & Wade (1999) discussed all available observations and found an inclination of $i = (45 \pm 20)^\circ$. This number has to be considered as quite uncertain.

Howarth & Prinja (1989) derived a radius of $R = 8 R_\odot$. With their error estimate, the maximum radius is about $R = 10.5 R_\odot$. Our value for $v \sin i$, although small, favors larger radii. Assuming $v \sin i = 29 \text{ km s}^{-1}$, which is about our lower limit for $v \sin i$ and yields convenient values, and an inclination angle of $i = 45^\circ$, we obtain $R = 12.5 R_\odot$. The minimum radius for an assumed $v \sin i = 29 \text{ km s}^{-1}$ is $R = 8.8 R_\odot$.

As a compromise we assumed a radius of $R = 10.2 R_\odot$ which for the fixed period leads to $i = 60^\circ$. In the following this set of parameters is called Model 1.

Alternatively, we investigated a model with $i = 45^\circ$ and $R = 12.5 R_\odot$. This is the set of parameters for Model 2.

It was shown by Stahl et al. (1996) that He and metal equivalent width curves are in phase. The time series of HeI λ 4471 and HeI λ 4713 are shown in Fig. 6. Since we do not know the broadening mechanism of Balmer and HeI lines we concentrate on the metal lines.

The assumption of local thermodynamic equilibrium in the model atmospheres used limits the applicability, especially in the case of the O6pe-star θ^1 Ori C. With the ATLAS9 model atmospheres which we used, it was not possible to calculate

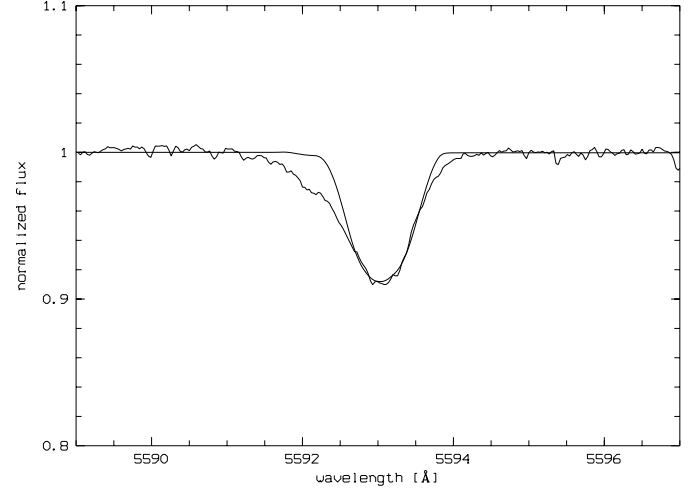


Fig. 5. Profile of the OIII λ 5592 line of θ^1 Ori C. A computed profile with the fitted value of 32 km s^{-1} for $v \sin i$ is overplotted. Note the strong wings in the observed profile which have not been taken into account in the fit since they do not show the shape of a rotational profile.

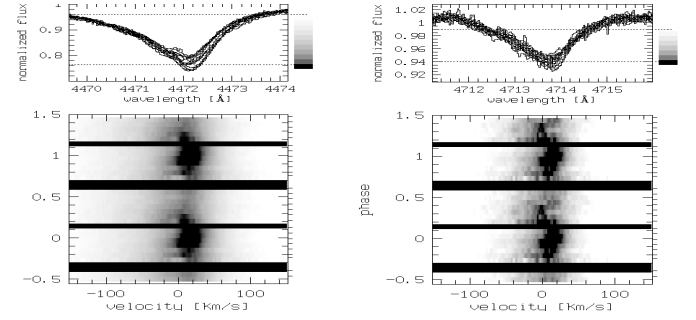


Fig. 6. Profiles of the HeI λ 4471 (left) and 4713 (right) lines of θ^1 Ori C versus phase. Phases are from -0.5 to 1.5 with a bin size of 0.06 . A velocity range of $\pm 150 \text{ km s}^{-1}$ around the rest wavelength is shown. Tick marks on the right border show phases where data has been taken.

model atmospheres for the effective temperature of θ^1 Ori C of $T_{\text{eff}} = 45\,500 \text{ K}$ (Howarth & Prinja 1989). We used an effective temperature of $T_{\text{eff}} = 39\,000 \text{ K}$ and $\log g = 4.2$. These are the parameters closest to θ^1 Ori C, where ATLAS9 models can still be computed.

Of course, we cannot expect to reproduce absolute values of the equivalent widths using these parameters. However, we believe that the qualitative behaviour of the line profiles and the relative strength of the equivalent widths due to abundance concentrations on the stellar surface can be reproduced reasonably well.

As described above, we synthesized series of spectral lines for the two models of θ^1 Ori C. Low abundance spots corresponding to a decentered dipole geometry turned out to be necessary – the spots do not lie exactly opposite each other. Thus we have four variables instead of two to parametrize the locations of the spots. Spectral lines of CIV, OIII and SiIV have been synthesized. The parameters are summarized in Table 4.

The equivalent width curve of CIV λ 5812 is shown in Fig. 7. In order to compare models and data, the equivalent widths are

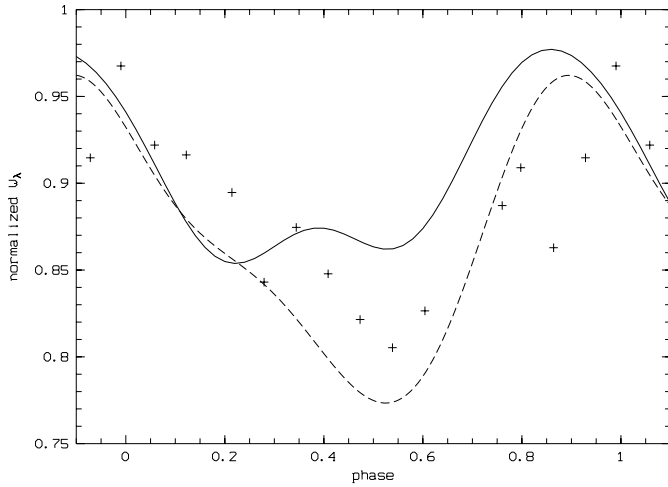


Fig. 7. Normalized equivalent width of the CIV λ 5812 line of θ^1 Ori C versus phase. The full line shows the equivalent width of Model 1, the dashed line of Model 2.

normalized to the same mean value in this figure. This was necessary as the model does not reproduce the absolute value of the equivalent widths. Data and model of the profiles of CIV λ 5812 and OIII λ 5592 versus phase are shown in Fig. 8.

The models are able to qualitatively reproduce the line shapes at all phases of the series reasonably well. The normalized equivalent width curves show the same tendency as the data. The two models can hardly be distinguished in the time series, but there are differences in the models' equivalent width curves. The models are not good enough to distinguish between the parameters, but if we take the average model, we derive the following values:

$$R = (11.4 \pm 1.2) R_{\odot} \quad (2)$$

$$i = (52 \pm 10)^{\circ} \quad (3)$$

$$v_{\text{rot}} = (38 \pm 3) \text{ km s}^{-1} \quad (4)$$

5.2. An equatorial spot model for θ^1 Ori C

Given the uncertainties of the model presented above – especially in the model atmospheres – the agreement with the observations is reasonably good. Nevertheless, we also investigated an alternative model with high abundance spots at the equator. The element distribution for such a model is roughly similar to the polar spot model, but it shows a different behaviour in the time series.

With such a model, we find a reasonable fit with the data if the spots are placed at $\vartheta_1 = 90^{\circ}$, $\varphi_1 = 0^{\circ}$ respectively $\vartheta_2 = 90^{\circ}$, $\varphi_2 = 260^{\circ}$. Radii are $r_1 = 50^{\circ}$ and $r_2 = 28^{\circ}$. Abundances are $\epsilon_0 = 8.5$ and $\epsilon_{\text{spot}} = 8.8$. A stellar radius of $R = 10.2 R_{\odot}$ was used for these calculations.

The normalized equivalent widths of this model are shown in Fig. 9. The agreement is remarkably good, but note that the equivalent widths are normalized to the same mean value.

Data and model of the profiles of CIV λ 5812 and OIII λ 5592 versus phase are shown in the right column of Fig. 8. It can be

Table 4. Parameters of the geometry of the models. Positions and sizes of the spots are the same for all three ions; within error-limits there is no need for an offset between them. Metals are depleted in the spots. For the assumed decentered dipole, ϑ and φ are necessary for both spots independently. One rotational pole is at $\vartheta = \varphi = 0$.

	Model 1			Model 2		
	CIV	OIII	SiIV	CIV	OIII	SiIV
i	60°			45°		
v_{rot}	35 $\frac{\text{km}}{\text{s}}$			41 $\frac{\text{km}}{\text{s}}$		
R	10.2 R_{\odot}			12.5 R_{\odot}		
φ_1	0°			0°		
ϑ_1	60°			45°		
φ_2	240°			240°		
ϑ_2	120°			140°		
r_1	20°			20°		
r_2	30°			55°		
ϵ_{spot}	6.4	5.8	7.0	6.4	5.8	7.0
ϵ_0	8.2	7.6	8.8	8.2	7.6	8.8

seen from this figure that the equatorial model produces line profile variations which fit the observations qualitatively better than the polar model. Both models fail to reproduce the line wings and the slight red-shift of the absorption feature crossing the lines.

6. Discussion

In Sect. 4, model calculations of the stellar atmosphere of σ Ori E have been presented. A good fit for the data has been obtained. Notably, the line profile variations versus rotational phase have been reproduced. The oblique rotator model presented by Groote & Hunger (1997) is confirmed for σ Ori E. We found an offset of $\Delta\varphi = 25^{\circ}$ between He- and metal-abundance spots on the stellar surface. This shows that our method for modeling stellar surfaces with local abundance variations actually works.

With this background, model calculations of θ^1 Ori C have been attempted. Low abundance spots at the pole and high abundance spots near the equator have been modeled. Both give a reasonable fit to the observations, but the equatorial spots give a better overall agreement with the observations.

For the classical Ap stars and He-variable stars two mechanisms for chemical fractionation are discussed: Diffusion (Michaud et al. 1976) in the atmosphere and stellar wind fractionation (Michaud et al. 1987). Diffusion requires a very stable atmosphere and therefore mass-loss is a process which competes with diffusion. According to calculations by Michaud (1992), diffusion does not operate for mass-loss rates above about $10^{-13} M_{\odot} \text{ yr}^{-1}$. This is much lower than the mass-loss rates of σ Ori E and θ^1 Ori C. Diffusion therefore is unlikely to contribute in these stars.

Stellar wind fractionation, on the other hand, seems to be able to explain the abundance pattern observed for He-rich and He-poor stars (Hunger & Groote 1999). The theory leads to predictions about enrichment and depletion of helium and metals

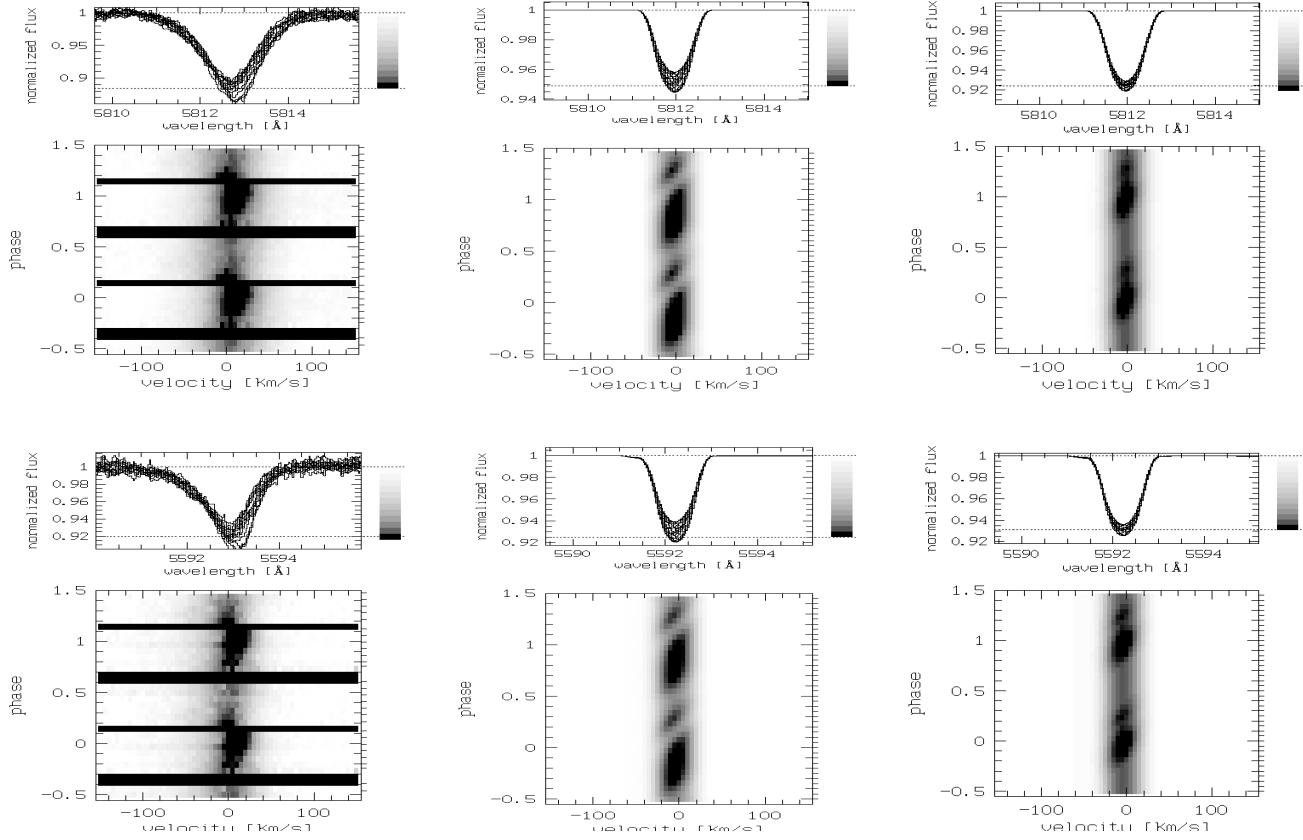


Fig. 8. Profiles of the CIV λ 5812 (top) and OIII λ 5592 (bottom) lines of θ^1 Ori C versus phase (left column: data, center column: polar spots (Sect. 5.1), right column: equatorial spots (Sect. 5.2)). Phases are from -0.5 to 1.5 with a bin size of 0.06 (data) and 0.05 (model). A velocity range of $\pm 150 \text{ km s}^{-1}$ around the rest wavelength is shown. Tick marks on the right border show phases where data have been taken.

at the poles, depending on the ionization of H and He in the stellar wind. Computations by Porter & Skouza (1999) indicate that stellar wind fractionation can operate up to maximum mass-loss rates of the order of $10^{-9} M_{\odot} \text{ yr}^{-1}$.

σ Ori E fits in this picture. He-rich and metal-poor caps are found to be located at nearly the same position. This behaviour is expected for stars with $T_{\text{eff}} = 22\,500 \text{ K}$. Hence we can identify the spots as poles of a magnetic dipole. This dipole coincides with the spectropolarimetric measurements of the magnetic field within the errors (Bohlender et al. 1987). A deviation from a centered dipole has been found, but we made no further efforts to investigate the detailed surface structure of σ Ori E.

For θ^1 Ori C we tried the same model geometry, assuming two abundance spots near the pole. He and metals are depleted in the spots. The spots do not lie opposite each other. If they are interpreted as magnetic poles, the magnetic field is decentered. This model could be interpreted in a similar way as for σ Ori E. Additionally, a model with a different abundance distribution has been investigated. In this model, we assume overabundant spots near the equator. The fit with observation is better in this case.

However, none of the known mechanisms for chemical fractionation is expected to work in the case of θ^1 Ori C. According to Howarth & Prinja (1989), the mass-loss rate of θ^1 Ori C is about $4 \cdot 10^{-7} M_{\odot} \text{ yr}^{-1}$. This makes diffusion an even more un-

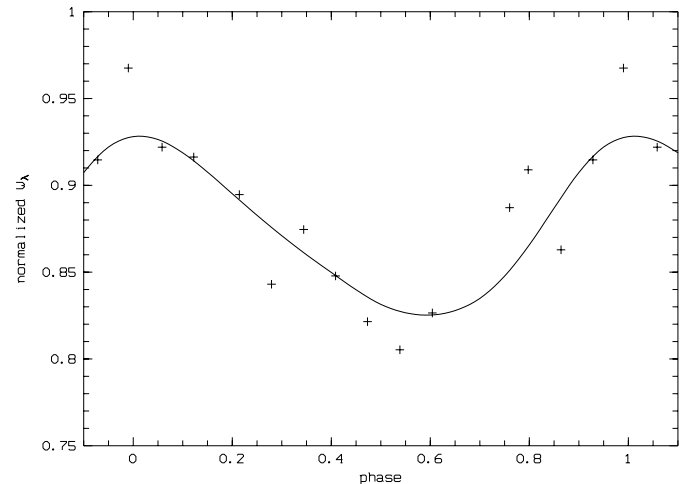


Fig. 9. Normalized equivalent width of the CIV λ 5812 line of θ^1 Ori C versus phase. The full line shows the equator spot model.

likely process for θ^1 Ori C than for σ Ori E. Also stellar wind fractionation is not expected to operate. This mechanism does not predict any fractionation if the temperature is higher than about $25\,000 \text{ K}$ (Hunger & Groote 1999). Also, the stellar wind is strong enough to prevent decoupling (Porter & Skouza 1999).

Therefore, another interpretation seems more plausible: Stahl et al. (1996) discussed the optical emission, UV absorption and photospheric absorption lines. They expected the UV absorption maximum at $\Phi = 0.5$ to originate from the magnetic pole, while the photospheric absorption and emission maxima are due to a region of enhanced density situated near the magnetic equator. This region may be related to the circumstellar disk predicted by Babel & Montmerle (1997).

The region of excess absorption in the high-velocity stellar wind in the UV is supposed to be located at the pole. It is shifted by $\Delta\Phi = 0.5$ with respect to the density enhanced region at the magnetic equator. In this scenario the shift can be explained: due to the inclination of the star and the obliquity of the magnetic field, we look straight at the magnetic equator with its density enhanced region at phase 0.0. At phase 0.5 one magnetic pole points directly in the direction of the observer.

The line profile variations of the optical absorption lines are interpreted in this model as variable excess absorption in the circumstellar environment and not as variations of the chemical abundance. The region where the excess absorption in θ^1 Ori C originates is a region of enhanced density on the magnetic equator. The emission lines have maximum strength at the same phase. This can naturally be explained, when the emission originates in the same region. A possible location for this region of enhanced density at the equator could be intersection points of the rotational and magnetic equator. σ Ori E also seems to have circumstellar matter in this region (Groote & Hunger 1997). The fact that we see the effects of this circumstellar matter in θ^1 Ori C even in the “photospheric” lines indicates a quite high density of circumstellar matter. This is also supported by the fact that the absorption line profiles are distorted (see e.g. Fig. 5 and the red-shift of the absorption feature in Fig. 8), indicating significant absorption from circumstellar matter.

Acknowledgements. We thank the DFG for support for the FEROS project at the Landessternwarte (Ap 19/6-1,6-2).

References

- Babel J., Montmerle T., 1997, ApJ 485, L29
 Barnard A.J., Cooper J., Smith E.W., 1974, J. Quant. Spectros. Rad. Transf. 14, 1025
 Baschek B., Holweger H., Traving G., 1966, Abhandl. Hamburger Sternwarte 8, 26
 Brandt J.C., 1970, Introduction to the Solar Wind. Freeman, San Francisco
 Bohlander D.A., Brown D.N., Landstreet J.D., Thompson I.B., 1987, ApJ 323, 325
 Donati J.-F., Wade G.A., 1999, A&A 341, 216
 Gagné M., Caillaut J.-P., Stauffer J.R., Linsky J.L., 1997, ApJ 478, L87
 Griem H.R., Baranger M., Kolb A.C., Oertel G., 1966, Phys. Rev. 125, 177
 Groote D., Hunger K., 1977, A&A 56, 129
 Groote D., Hunger K., 1982, A&A 116, 64
 Groote D., Hunger K., 1997, A&A 319, 250
 Hesser J.E., Moreno H., Ugarte P., 1977, ApJ 216, L31
 Howarth I.D., Prinja R.K., 1989, ApJS 69, 527
 Hunger K., Heber U., Groote D., 1989, A&A 224, 57
 Hunger K., Groote D., 1999, A&A 351, 554
 Kaufer A., Szeifert Th., Krenzin R., Baschek B., Wolf B., 1994, A&A 289, 740
 Kaufer A., Wolf B., Andersen J., Pasquini L., 1997, ESO Messenger 89, 1
 Kaufer A., 1998, Fiber Optics in Astronomy III, ASP Conf. Series 152, 337
 Kaufer A., Pasquini L., 1998, Proc. SPIE 3355, 844
 Kurucz R.L., 1979, ApJS 40, 1
 Kurucz R.L., 1993, In: Dworetzky M.M., Castelli F., Faraggiana R. (eds.) Peculiar versus normal phenomena in A-type and related stars. IAU Coll. 138, ASP Conf. Series, p. 87
 Mihalas D., Conti P.S., 1980, ApJ 235, 515
 Michaud G., Charland Y., Vauclair S., Vauclair G., 1976, ApJ 210, 447
 Michaud G., Dupres J., Fontaine G., Montmerle T., 1987, ApJ 322, 302
 Michaud G., 1992, In: Heber U., Jeffery C.S. (eds.) The atmospheres of early-type stars. Lecture Notes in Physics 401, p. 189
 Mukai K., 1990, PASP 102, 183
 Porter J.M., Skouza B.A., 1999, A&A 344, 205
 Stahl O., Wolf B., Gäng Th., et al., 1993, A&A 274, L29
 Stahl O., Kaufer A., Rivinius T., et al., 1996, A&A 312, 539
 Stahl O., Kaufer A., Tubbesing S., 1999, ASP Conf. Series 188, 331
 Townsend R., 1997a, Dissertation, University College London
 Townsend R., 1997b, MNRAS 284, 839
 von Zeipel H., 1924, MNRAS 84, 665
 Walborn N.R., Nichols J.S., 1994, ApJ 425, L29